Semidiurnal currents in the Arctic Ocean's eastern Eurasian Basin

Till M. Baumann[1,4], Igor V. Polyakov[1], Laurie Padman[2], Seth Danielson[3], Ilker Fer[4], Susan Howard[2], Jenny Hutchings[5], Markus Janout[6], An Nguyen[7], Andrey V. Pnyushkov[8]

[1]International Arctic Research Center and College of Natural Science and Mathematics, University of Alaska Fairbanks (UAF), Fairbanks, AK, USA and Finnish Meteorological Institute, Helsinki, Finland
[2]Earth & Space Research, Corvallis, OR, USA
[3]College of Fisheries and Ocean Sciences, UAF, Fairbanks, AK, USA
[4]Geophysical Institute, University of Bergen and Bjerknes Centre for Climate Research, Bergen, Norway
[5]College of Earth, Ocean and Atmospheric Sciences, Oregon State University, Corvallis, OR, USA
[6]Alfred Wegener Institute Helmholtz Centre for Polar and Marine Research, Bremerhaven, Germany
[7]University of Texas at Austin, Institute for Computational Engineering and Sciences, Austin, TX, USA
[8]International Arctic Research Center, UAF, Fairbanks, AK, USA

Key Points:

- Semidiurnal-band mean current speeds are 33-71% of mean total current speed across the continental slope
- During ice-free summers, wind-driven inertial currents typically exceed 30 cm/s in the upper 30 m throughout the study region
- During winters, baroclinic semidiurnal tidal currents dominate and can be vigorous ($\sim$ 20 cm/s) over the continental slope

Corresponding author: Till Baumann, `till.baumann@uib.no`

Abstract

In the Arctic Ocean, semidiurnal-band processes including tides and wind-forced inertial oscillations are significant drivers of ice motion, ocean currents and shear contributing to mixing. Two years (2013-2015) of current measurements from seven moorings deployed along 126° E from the Laptev Sea shelf (∼50 m) down the continental slope into the deep Eurasian Basin (∼3900 m) are analyzed and compared with models of baroclinic tides and inertial motion to identify the primary components of semidiurnal-band current (SBC) energy in this region. The strongest SBCs, exceeding 30 cm/s, are observed during summer in the upper ∼30 m throughout the mooring array. The largest upper-ocean SBC signal consists of wind-forced oscillations during the ice-free summer. Strong barotropic tidal currents are only observed on the shallow shelf. Baroclinic tidal currents, generated along the upper continental slope, can be significant. Their radiation away from source regions is governed by critical latitude effects: the S_2 baroclinic tide (period = 12.000 h) can radiate northwards into deep water but the M_2 (∼12.421 h) baroclinic tide is confined to the continental slope. Baroclinic upper-ocean tidal currents are sensitive to varying stratification, mean flows and sea ice cover. This time-dependence of baroclinic tides complicates our ability to separate wind-forced inertial oscillations from tidal currents. Since the shear from both sources contributes to upper-ocean mixing that affects the seasonal cycle of the surface mixed layer properties, a better understanding of both inertial motion and baroclinic tides is needed for projections of mixing and ice-ocean interactions in future Arctic climate states.

Plain Language Summary

Currents created by winds and tides are important contributors to ocean mixing and influence how the ocean and sea ice interact in the Arctic Ocean. In the eastern Arctic, the strongest currents from both sources oscillate with a period of about 12 hours (i.e., "semidiurnal"). We analyse ocean current speed and direction measurements taken between 2013 and 2015 from the Arctic Ocean's Eurasian Basin along a line near longitude 126°E that extends from shallow to deep water. Separating contributions from wind and tides is difficult, so we also use numerical model simulations to help interpret the observational data. During ice-free summer months, currents with close to 12-hour periods in the upper ocean are dominated by wind-driven flows, often exceeding 30 cm/s at depths down to 30 m below the surface. During winter months, tidal currents that

vary in both depth and time dominate the semidiurnal currents. Such currents can be vigorous over the continental slope and change their vertical extent with the seasonal change of water density. These motions potentially foster mixing of waters far below the ocean surface.

1 Introduction

The Eurasian Basin (EB) of the Arctic Ocean comprises the Nansen Basin and Amundsen Basin (Figure 1). Our study region is confined to east of Severnaya Zemlya (∼95°E) and is characterized by a continental slope ascending from the abyssal plain (∼3900 m) to the shallow Laptev Sea shelf (∼50 m). We refer to this whole region (comprising the deep basin, continental slope and Laptev Sea shelf) as "eastern EB". The hydrography in the eastern EB continental slope region is strongly affected by the Arctic Circumpolar Boundary Current (ACBC). Atlantic Water enters the Arctic Ocean through Fram Strait and the Barents Sea and is carried by the ACBC cyclonically along the continental margins and ridges of the Arctic Ocean at intermediate depths of about 200-1000 m (Timofeev, 1960; Coachman & Barnes, 1963; Aagaard, 1989; Rudels et al., 1994; Pnyushkov et al., 2018); see Figures 1 and 2.

Ocean mixing processes in the EB help determine the fate of AW heat within the Arctic, including its spread into the western Arctic and its potential to influence the upper ocean and sea ice. Substantial changes in stratification have been observed in the eastern Arctic Ocean in recent years, associated with increasing importance of Atlantic Water inflows (Polyakov et al., 2017). This "atlantification" of the eastern Arctic coincides with increases in current speeds and velocity shear in the basin, which are associated with a regime change from a calm double-diffusive to a more vigorous shear-driven mixing environment (Polyakov et al., submitted). These changes may play a direct role in the observed reduction of sea ice volume and an indirect role through feedbacks (e.g., Carmack et al., 2015).

Turbulent mixing, below the well-mixed surface layer, is driven by shear instabilities. In the eastern Arctic, much of the shear can be attributed to semidiurnal-band baroclinic waves (Polyakov et al., submitted), either tides or wind-forced near-inertial motion. Observations of semidiurnal currents from Arctic Ocean moorings reveal strong seasonal variability related to changes in the sea ice cover (Rainville & Woodgate, 2009; Pnyushkov

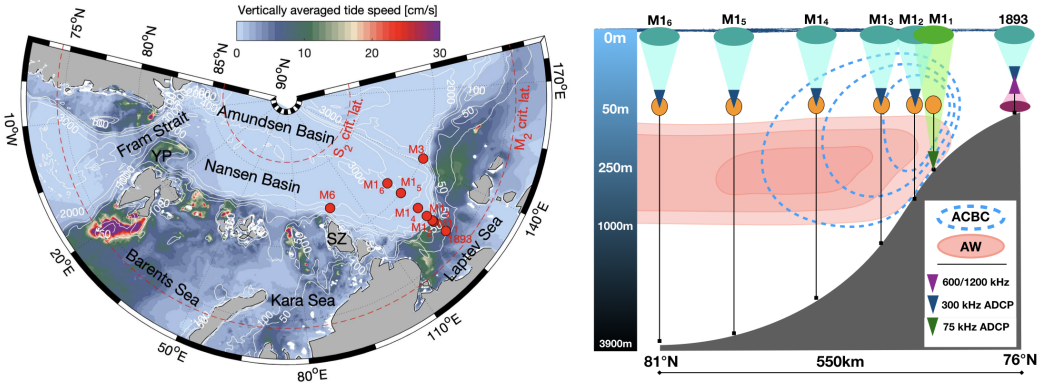

Figure 1. Left: Map showing vertically averaged barotropic tidal current speed from the inverse barotropic tidal model of Padman and Erofeeva (2004) for the Atlantic side of the Arctic Ocean. Dashed red lines indicate the critical latitude of the S_2 and M_2 constituents. White lines and labels show isobaths. Red dots indicate the positions of moorings whose data are used in this study. YP = Yermak Plateau, SZ = Severnaya Zemlya. Right: sketch (not to scale) of the moorings comprised in the section along 126°E and their approximate location relative the Atlantic Water (AW) layer and the Arctic Circumpolar Boundary Current (ACBC).

& Polyakov, 2012). Models of baroclinic tides generated by barotropic tidal flow over steep and/or rough bathymetry indicate that tidal currents are also sensitive to background stratification and currents. These prior studies suggest that changes in sea ice cover, stratification and circulation in the eastern Arctic could cause substantial changes in the intensity of shear instabilities and the associated turbulent mixing.

As a step towards a better understanding of future changes in eastern Arctic current dynamics, we investigate the sources and variability of upper-ocean semidiurnal-band kinetic energy across the eastern EB continental slope. The paper is organized as follows. In section 2 we summarize our present knowledge of Arctic tidal currents and wind-forced inertial motion, and their contributions to the state of the Arctic ocean and ice system. We then describe a data set of upper-ocean currents collected in the eastern EB during 2013-2015, and the analysis methods we use to discuss contributions to the semidiurnal band variability (section 3 and 4). The results of the tidal analysis are presented

in section 5. In section 6, we discuss the results, including shortcomings of classical harmonic tidal analysis. The summary of our findings is provided in section 7.

2 Tidal and wind-forced inertial currents in the Arctic

Variability of semidiurnal band currents (SBCs) and associated mixing processes in the upper Arctic Ocean has usually been attributed to wind-driven inertial currents that depend directly on sea ice cover and changes in wind stress (e.g., Rainville & Woodgate, 2009; Martini et al., 2014; Fer, 2014). For some portions of the Arctic continental shelves and slopes, however, tidal variability may also play a substantial role: for a record from the Beaufort Sea shelf, Kulikov (2004) found that the tidal contribution to the observed signal is variable in space and time, reaching up to 74% of the total signal.

2.1 Tides

Tidal currents can be partitioned into barotropic and baroclinic components, with the barotropic currents representing the component that would be present in a homogeneous ocean with a free surface, and baroclinic currents being associated with the presence of stratification. Barotropic tidal currents vary regionally (Figure 1) but are relatively uniform over time and depth.

Where barotropic tidal currents flow across steep slopes or rough topography in the presence of stratification, energy can be converted from barotropic to baroclinic (internal) tides whose energy finally dissipates in mixing processes (e.g., Wunsch, 1975; Simmons et al., 2004). For baroclinic tides, the processes of generation, propagation and dissipation are sensitive to stratification, mean flow, and energy losses through friction and mixing within the water column.

Baroclinic tidal waves cannot freely propagate poleward of their critical latitude, the latitude at which their frequency equals the local inertial frequency (e.g., Prinsenberg & Bennett, 1989). For diurnal tides, this latitude is roughly 30°, and all baroclinic diurnal energy in the Arctic is trapped to the "wave guide" of the continental slope (Kowalik & Proshutinsky, 1993). The critical latitude for the dominant semidiurnal tide M_2 (period ∼12.421 h) is ∼74.5°N and for S_2 (period of 12.000 h) it is ∼86°N. Most of the EB continental slope is between these latitudes (see Figure 1), meaning that baroclinic S_2 tides generated along the slope can propagate freely across-slope but M_2 cannot. In-

stead, M_2 energy either radiates along the slope Hughes:2019iu or is dissipated locally through mixing or nonlinear energy transfers to high frequency waves (e.g., Falahat & Nycander, 2015; Rippeth et al., 2017; Kozlov et al., 2017).

Regions of elevated tidal energy along the continental shelf edges generally coincide with the pathway of Atlantic Water in the ACBC through the eastern Arctic. The phenomenon of tidal energy conversion and turbulent mixing has been studied in detail near the Yermak Plateau, north of Svalbard (e.g., Padman et al., 1992; Fer et al., 2010, 2015). There, intense tide-forced mixing cools and freshens the incoming AW. Holloway and Proshutinsky (2007) proposed, based on a general circulation model with a relatively simple parameterization of tidal friction at the seabed, that tides are a critical component of mixing responsible for setting the distributions of Atlantic Water hydrographic properties throughout the Arctic. Limited microstructure measurements obtained across the Arctic Ocean between 2007 and 2013 support this view of tidally driven mixing along the continental margins. The dissipation rate strongly depends on the steepness of the continental slope, which decreases in the eastward direction along the Atlantic Water path (Rippeth et al., 2015). However, Lenn et al. (2011) found intense tidally driven mixing far east on the continental shelf of the Laptev Sea, in a region where Janout and Lenn (2014) found strong M_2 tidal currents (up to $\sim$30 cm/s) that experienced substantial seasonal changes as stratification varied. Pnyushkov and Polyakov (2012) reported that, further offshore over the continental slope at mooring $M1_4$ at 2700 m bottom depth (see Figure 1 for location), semidiurnal-band currents in the upper ocean were weak (O(1) cm/s) in winter but increased to $>$8 cm/s during ice-free summer months. Those authors attributed the seasonal variability to changes in baroclinic tides as sea ice and stratification changed with time.

The interactions between sea ice cover and tides are complex. For high-concentration pack ice, the ice provides a frictional boundary that may increase energy dissipation (Morison et al., 1985), potentially leading to a deepening of the surface mixed layer (Padman et al., 1992). For low-concentration or easily deformed thin ice, however, reported effects on tidal currents and associated dissipation range from negligible (e.g., Danielson & Kowalik, 2005; Rippeth et al., 2015) to substantial (e.g., Pnyushkov & Polyakov, 2012).

2.2 Wind-forced inertial currents

The inertial frequency is the natural frequency of sea ice and ocean current responses to changes in wind stress. The efficiency of the transfer of momentum from atmosphere to ocean depends on the presence and properties of sea ice. From ice tethered profiler data, Cole et al. (2018) found that the energy of the internal wave field generated by inertial motions is weakest for ice cover near 100% and abruptly increases once sea ice concentration drops below ∼80%. Inertial internal waves below the surface mixed layer (SML) can propagate freely and eventually dissipate, redistributing wind energy through the water column (Munk & Wunsch, 1998). Although the Arctic Ocean is historically known as having relatively low wind-forced total internal wave energy (Levine et al., 1985), evidence for the importance of inertial motions in the Arctic is well documented from measurements of ocean currents (e.g., Rainville & Woodgate, 2009; Fer, 2014; Martini et al., 2014) and sea ice drift (e.g., Gimbert et al., 2012). Observations suggest increases in variability and amplitude of the near-inertial wave field in recent years, which are mostly attributed to the widespread reduction of sea ice cover and thickness (Dosser & Rainville, 2016).

3 Data

3.1 The 126°E Mooring array

The principal dataset used in this study consists of moored observations from the Nansen and Amundsen Basin Observational System (NABOS) project (`https://uaf-iarc.org/NABOS/`). An array of six moorings ($M1_1$–$M1_6$) along the 126°E meridian from just offshore of the Laptev Sea shelf (∼77°N; 250 m water depth) to the abyssal plain (∼81°N; 3900 m depth) was deployed for two years from September 2013 to September 2015 (Figure 1, see Table 1 for bottom depth at each mooring). All moorings were designed to obtain profiles of velocity (u(t,z), with orthogonal components u (eastward) and v (northward)) over limited depth ranges (see Table 1), and measurements of temperature and salinity at fixed depths. Velocities were obtained at hourly resolution for the upper ∼50 m using 300kHz acoustic Doppler current profiler (ADCP) instruments at all but two moorings: $M1_1$, where a 75kHz ADCP moored near the seabed was used to capture velocities throughout most of the water column; and $M1_5$, which missed its target depth

and was deployed ∼30 m too deep. The ADCPs generally returned full 2-year data records; however, the ADCP at $M1_5$ stopped working after about 10 months.

Manufacturer-provided accuracies for speeds and directions are ±0.5 cm/s and ±2° for vertical averaging bin sizes of 2 m and 5 m for the 300kHz and 75kHz ADCPs, respectively. Signals from all ADCPs were contaminated close to the surface by surface reflections of sidelobe energy. For the upward-looking 300kHz ADCPs moored near 50 m depth, the upper 8 m could not be used; for the 75kHz ADCP mounted at ∼250 m depth at $M1_1$, the top 30 m was discarded.

The NABOS mooring array was supplemented by mooring 1893, deployed in September 2013 on the Laptev Sea shelf in ∼50 m water depth near 76°N, 126°E, within the German-Russian "Laptev Sea System" partnership during the *Transdrift 21* expedition. The mooring was recovered and redeployed in 2014 during *Transdrift 22* to obtain an additional year of data. Both deployments carried an upward-looking 300kHz ADCP at 35 m (2013) and 37 m (2014) depth, and downward-looking, higher frequency-instruments (600kHz mounted at 30 m in 2013 and 1200kHz at 35 m in 2014) to resolve the near-bottom part of the water column.

3.2 Sea ice and atmospheric conditions

Local sea ice concentration and 10-m winds at each mooring location were obtained from ERA5 reanalysis output (Copernicus Climate Change Service, 2017), which has a grid spacing of 0.25° and temporal output of 1 h.

4 Methods

4.1 Semidiurnal-band currents

In order to quantify the properties and spatio-temporal changes in the semidiurnal band current (SBC) energy, we band-passed the current records to retain only signals between 10-h and 14-h periods; this gives an effective modulation time scale of about 36 h. We performed the filtering with an 8^{th} order band-pass Butterworth filter on half overlapping 1-year windows (except for $M1_5$ where we used a shorter window length of ∼1/2 year), applied separately to the u and v components.

4.2 Harmonic tidal analysis

We analyzed the current velocities using the T_TIDE Matlab toolbox (Pawlowicz et al., 2002), which is based on methods described by Foreman (1978). T_TIDE performs a harmonic analysis based on known frequencies for up to 69 tidal constituents (for records of 12 months or longer) and calculates tidal ellipse parameters (major and minor axis amplitudes, orientation, rotation direction, and phase), and confidence intervals for each parameter.

In most ocean environments, the bulk of the total tidal variance is in eight constituents, four semidiurnals (M_2, S_2, K_2, N_2) and four diurnals (O_1, K_1, P_1, Q_1). Formal separation of these eight constituents requires about 183 days (six months) of hourly data (see Table 3 in Padman et al. (2018)). Tidal analyses on shorter records (e.g. 30 days, as commonly available from temporary tide gauge deployments, and as used in our study to capture temporal variability of tidal currents), report the combination of S_2 and K_2 as S_2only, while K_1 and P_1 are reported as K_1. For barotropic tide heights, where amplitudes and phases are stable in time, these pairs can be separated in short records by "inference" (Foreman, 1978; Pawlowicz et al., 2002). In the present analysis, however, we expect that much of the tidal energy is in time-varying baroclinic modes where assumptions required for inference may not apply. For analysis of short records, we therefore define the inseparable sum of S_2 and K_2 as S_2* and the sum of K_1 and P_1 as K_1*.

All tidal analyses presented in this study are based on the application of T_TIDE to 30-day windows (sliding at 1-h increments), run over the whole record at each depth level. This analysis yields a full set of tidal ellipse parameters at the same time and depth coordinates as the raw hourly data, excluding the first and last 15 days of each record. T_TIDE also provides a "tidal prediction", derived from the summation of currents for all tidal constituents with sufficiently high signal-to-noise ratio. We refer to the east and north components of these currents as $u_{\text{T\_TIDE}}$ and $v_{\text{T\_TIDE}}$, respectively. The resulting time series of speed is then $|u|_{\text{T\_TIDE}} = ({u_{\text{T\_TIDE}}}^2 + {v_{\text{T\_TIDE}}}^2)^{1/2}$, with subscripts reminding the reader that these are not necessarily true tidal currents but are the tidal reconstructions from the T_TIDE analyses.

4.3 Estimating wind-driven inertial currents in the surface mixed layer

We used a damped slab model (Pollard & Millard Jr, 1970; D'Asaro, 1985) to estimate the wind-driven inertial currents in the SML. This model provides the time evolution of the SML current vector for a given time series of vector wind stress, specified SML depth and a decay constant representing damping terms including dissipation and energy losses through internal wave radiation. The temporal resolution of the wind stress has a substantial influence on the generation of inertial currents. For mid-latitudes, D'Asaro (1985) found that the energy flux from wind to inertial motions is underestimated by $\sim$20% using 3-hourly wind data, whereas for hourly wind data this error is only $\sim$2%. Thus, we regard hourly output of wind velocity from ERA5 (section 3.2) as being adequate to generate an inertial response. Changes in both amplitude and direction of the wind stress vector can excite or dampen resonant motions. We followed Andreas et al. (2010) to account for the effect of sea ice concentration on wind stress penetration into the ocean using concentration values from the ERA5 reanalysis at the grid points closest to each mooring site. Distances of the closest grid point are always less than 13 km. The damping time scale is usually taken to be in the range of 2 to 14 days (D'Asaro, 1985). In an Arctic application, Martini et al. (2014) used a damping time scale of 3.5 days in the Beaufort Sea based on theoretical considerations described by Alford (2001). To obtain results likely to be at the higher end of realistic inertial currents, we made computations using a shallow mixed layer depth (10 m) and a long decay time scale (14 days). We expect that uncertainties in ERA5 winds due to the paucity of data constraints in the eastern Arctic may further contribute to uncertainties in predicted SML inertial currents.

4.4 Modeling three dimensional tidal currents

We used the Regional Ocean Modeling System (ROMS) version 3.7 (Haidvogel et al., 2000; Shchepetkin & McWilliams, 2005) to study tidal currents and the differences in the behavior of semidiurnal constituents M_2 and S_2. ROMS is a hydrostatic 3-D primitive equation model using a terrain-following (sigma-level) coordinate system. Our model covers the Eastern Arctic region with 51 vertical levels on a horizontal grid with spacing of 2 km. The bathymetry was based on IBCAO version 3 (Jakobsson et al., 2012) and smoothed to a Beckmann and Haidvogel number (rx0) of 0.2 to reduce pressure gradient errors (Beckmann & Haidvogel, 1993).

The model was forced at the open boundaries with both tidal currents and elevation values from the Arctic Ocean 5 km forward model (AODTM-5) developed by Padman and Erofeeva (2004). No atmospheric forcing was imposed. The initial conditions (stratification and background currents) were taken from a 4-km, 90-level ocean and sea ice Arctic Ocean simulation using the community ocean model MITgcm (Marshall et al., 1997; Losch et al., 2010). This Arctic simulation used hydrographic data from release 1 of the Arctic Subpolar gyre state Estimate, ASTE (Nguyen et al., 2017). We used simulated 2014 mean-March and mean-September modeled fields, interpolated to our ROMS grid, to represent winter and summer conditions, respectively. We tested for errors associated with interpolation and the ROMS grid structure by conducting no-forcing runs to ensure that the background conditions did not vary significantly from initial conditions over the course of a tidal run.

We ran multiple 20-day simulations, forced with M_2 and S_2 separately, to examine differences in behavior of the semidiurnal tides due to seasonal changes in stratification and circulation, and the maximum likely effect of adding sea ice to winter stratification. Ice was applied as a thin plate of land-fast ice at 100% concentration to add friction at the ocean surface. No thermodynamic exchanges between ocean and ice were modeled.

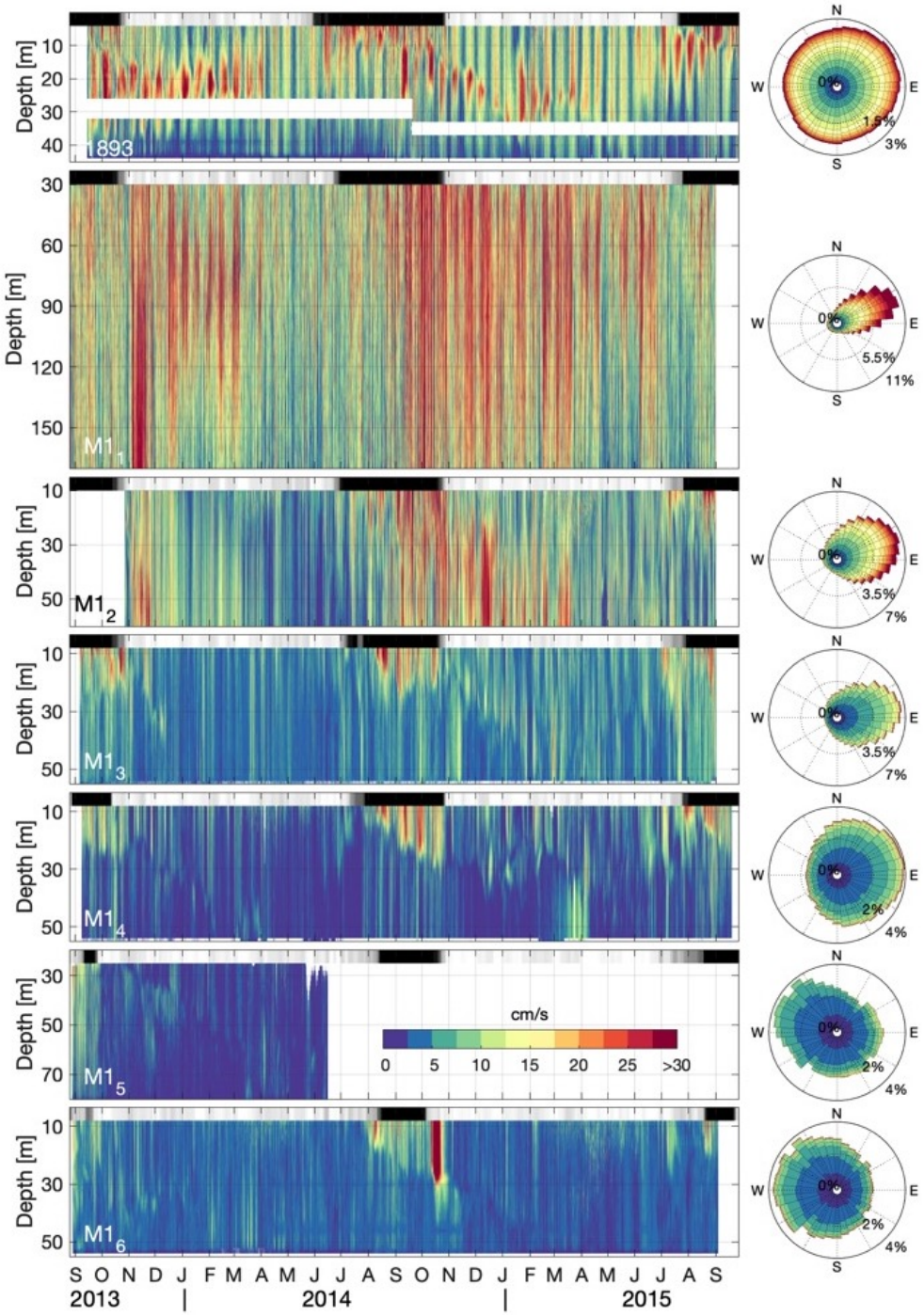

Figure 2. (Left column) Time-depth plots of observed currents speed at the mooring locations shown in Fig. 1. Gray shading at the top of the plots indicates sea-ice concentration (white= 100% , black= 0%). (Right column) The distribution of direction (the length of each 10° bin is proportional to the percentage of data within this bin) and amplitude (colors) of the observed currents.

5 Results

5.1 Current velocities

Variability of hourly total current speeds along the 126°E mooring array was large in both time and space (Figure 2). At mooring 1893 on the shelf, speeds were high throughout the two years, with no dominant direction. Speeds varied with a roughly 2-week cycle and the depth of maximum current speed varied on an annual cycle, being shallowest in the summer period when no sea ice was present. Further down the slope (moorings $M1_1$ and $M1_2$), velocities were generally directed slightly north of east, consistent with these moorings being within the core of the ACBC (e.g., Pnyushkov et al., 2015). North of mooring $M1_2$, the directional coherence and average velocity decreased with increasing distance offshore (moorings $M1_3$ to $M1_6$). However, at the offshore moorings there were pronounced summertime velocity amplifications, especially in August to late October in 2014. These summer maxima became stronger with increasing distance offshore. The largest current speed in the offshore moorings exceeded 30 cm/s for a short period in October 2014 at mooring $M1_6$.

Table 1. Tidal ellipse parameters for four constituents at all moorings across the array. Values are averaged over time and depth (see last columns for depth ranges and bottom depth). Italic font for major axis amplitudes indicates amplitudes at or below 95% confidence level. For Eccentricity, italic font indicates that major axis amplitude and/or minor axis amplitude are at or below 95% confidence level.

	Depth range [m]	Bottom depth [m]	U_{maj} [cm/s]				Eccentricity				Orientation [° from East]				Phase [° from Greenwich]			
			M_2	S_2*	K_1*	O_1	M_2	S_2*	K_1*	O_1	M_2	S_2*	K_1*	O_1	M_2	S_2*	K_1*	O_1
1893	4-44	50	6.7	4.1	1.8	*1.4*	1.2	1.3	*2.3*	*2.4*	49	62	113	106	267	270	206	215
$M1_1$	30-230	250	4.3	2.6	*1.5*	*1.4*	1.4	1.6	*2.8*	*3.5*	97	94	75	82	254	249	136	172
$M1_2$	10-60	790	5.3	3.8	1.3	*1.0*	1.4	1.5	*3.6*	*3.5*	86	101	95	92	251	293	151	166
$M1_3$	8-48	1850	2.9	2.6	*0.6*	*0.6*	1.2	1.2	*3.3*	*3.5*	63	102	93	89	242	226	179	177
$M1_4$	8-50	2720	2.2	2.3	*0.5*	*0.6*	1.4	1.3	*3.4*	*3.3*	83	76	95	84	206	229	177	191
$M1_5$	25-82	3440	1.2	2.1	*0.2*	*0.2*	*2.1*	1.3	*3.2*	*3.1*	96	132	87	91	207	285	183	171
$M1_6$	8-46	3900	1.5	2.1	*0.5*	*0.5*	*2.1*	1.3	*3.3*	*3.4*	91	106	89	89	204	240	176	187

Rotary spectra of the depth-averaged (see Table 1 for depth ranges) velocities for each mooring time series show that, in general, the power in the clockwise component surpassed that of the counter-clockwise component (Figure 3). These spectra were obtained from averaging of 50% overlapping windows of 1/3 the length of each time series; for a 2-year record, a spectrum represents oscillatory signals that remain stationary for ∼8 months. The preferred polarization of current ellipses is determined by the Earth's rotation (e.g., Gonella, 1972). The highest energy density for each mooring is in the semidiurnal band, with distinct peaks centered at frequencies for the M_2, S_2, and N_2 constituents. Peak power is highest at M_2 for all moorings over the slope and shelf (onshore of, and including mooring $M1_4$); however, the greatest power at the offshore moorings $M1_5$ and $M1_6$ is at S_2. The peaks become broader in frequency with increasing distance offshore, indicative of increasing baroclinicity (e.g., Munk, 1997; Kulikov, 2004). We attribute the lack of distinct power peaks at the inertial to time variability of wind events leading to a lack of phase coherence of wind-forced near-inertial oscillations throughout each entire mooring record. For the dominant diurnal constituents, K_1 and O_1, peaks are only distinguishable at the inshore moorings 1893 and $M1_1$. A little further down the slope, at $M1_2$, only K_1 is identifiable (Figure 3). In further analyses, we focus on the semidiurnal current variability.

5.2 Semidiurnal-band and total tidal currents

Averaged over time and depth, the mean speed of semidiurnal-band currents (SBCs) is 53% of the mean measured current speed across the array (Table 2). Values at the individual mooring sites range from 33% for mooring $M1_1$, where the flow of the ACBC is substantial, to 71% at mooring 1893 on the shelf, where background flow is weak (Figure 2).

SBCs exhibit substantial variability with depth and on a broad range of time scales including seasonal and fortnightly frequencies (Figure 4, left column). The strongest SBCs are almost always in the upper 30 m in late summer 2014 and reach peak velocities of 49 cm/s in October 2014 at the offshore mooring $M1_6$. The summer signals follow a pattern of progressive deepening over the course of the ice-free season; strong currents are confined to the upper limit of observations (∼10 m) at the onset of ice melt (June-July), then gradually deepen to about 30 m by late October. This pattern is typical of the impact of wind forcing on seasonally ice-free seas (e.g., Rainville & Woodgate, 2009), where

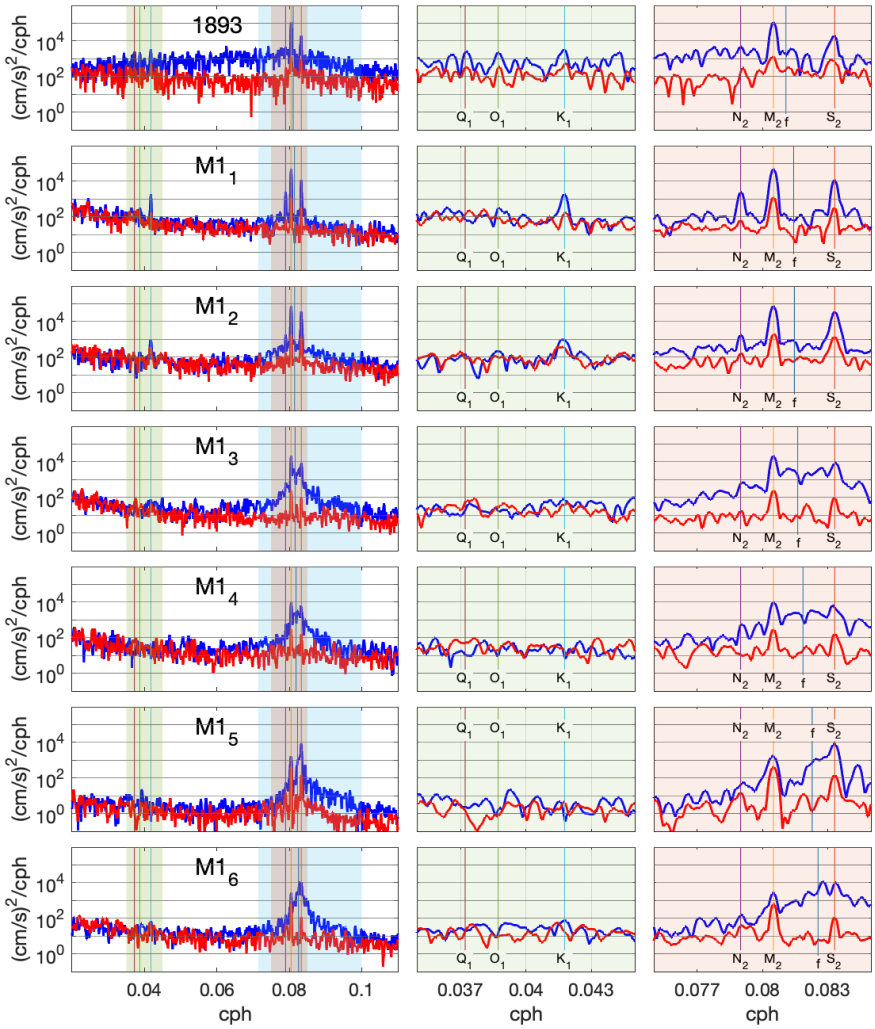

Figure 3. Left column: Rotary spectra (using Welch's method with window length of 1/3 of the length of the time series and 50% overlap) of depth-averaged velocities. Blue indicates the clockwise component, red the counter-clockwise component. Middle and right columns are zoomed-in on diurnal (green shading) and semidiurnal (red shading) frequency bands, respectively. Colored lines and labels mark the frequencies of the dominant tidal constituents as well as local inertial frequency (f). Blue shading in the left column indicates the frequency band (10-14 h period) used for the band-pass filtered semidiurnal band currents.

rapid sea ice melting in early summer creates a shallow, strongly-stratified SML that deepens by mixing through summer once the primary source of surface buoyancy is removed. The fact that the maximum at $M1_6$ is observed apparently after sea ice has formed again

is thus surprising and might be associated to uncertainties in the sea ice reanalysis product.

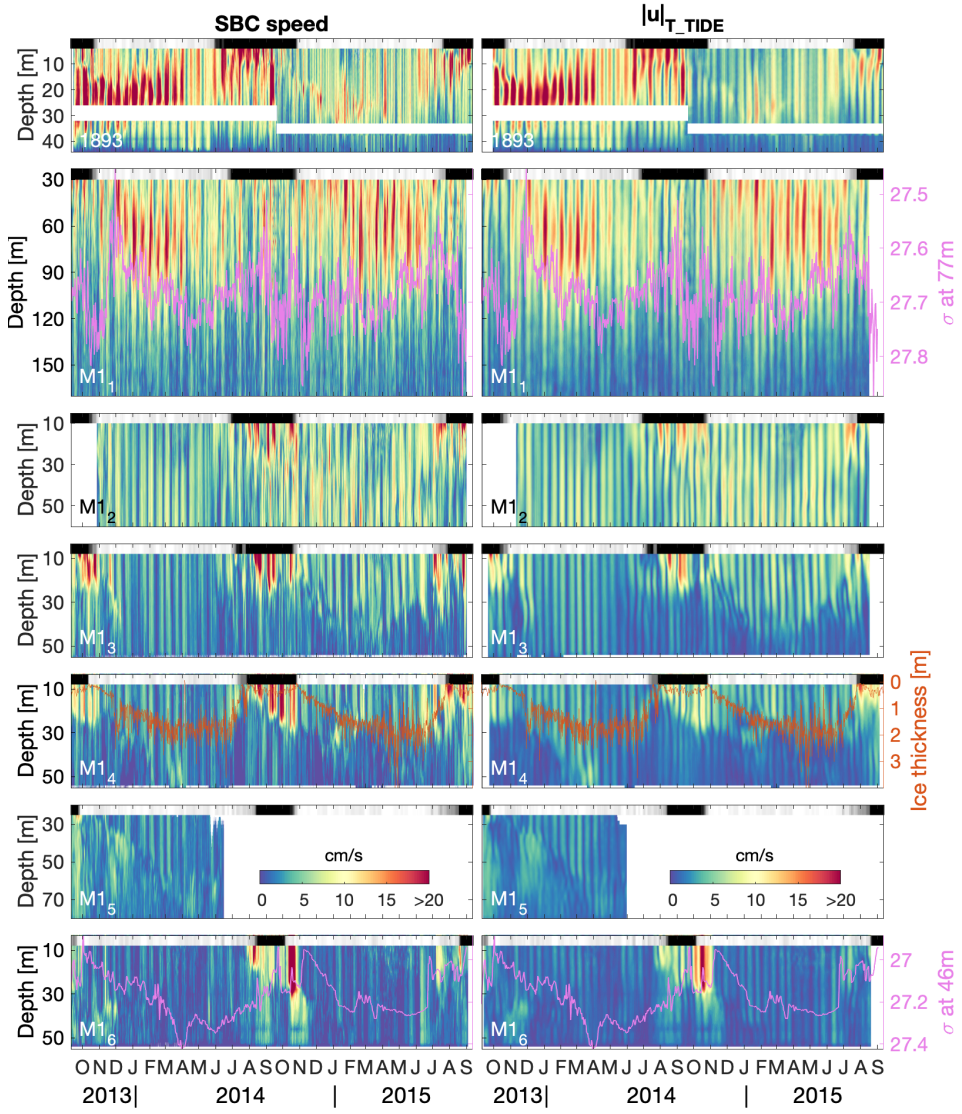

Figure 4. Left column: 10-14 h band pass filtered raw speed, representing near-inertial currents (SBCs). Right column: Total tidal current speed as derived from T_TIDE analysis ($|u|_{\text{T\_TIDE}}$). The fortnightly modulation of the signal stems from the superposition of the constituent pairs S_2* and M_2, and K_1* and O_1.

The prominent higher-frequency variability in SBC speed often has a period of about two weeks, consistent with expectations from the spring-neap modulation of the dominant semidiurnal tidal constituents M_2 and S_2 identified in spectra (Figure 3). However, the modulation period can vary, in some depth ranges for some moorings, in the range

∼1-4 weeks. We attribute this variability to two factors; the addition of wind-forced inertial currents with timescales set by passage of weather systems, and broadening of tidal spectral peaks (Figure 3) by the sensitivity of baroclinic tides to changing ocean background state.

Based on the presence of semidiurnal and diurnal tidal peaks in spectra (Figure 3) and the roughly fortnightly (apparently spring-neap) modulation of SBCs, we carried out tidal analysis as described in section 4.2 Plots of total tidal current speed ($|u|_{\mathrm{T\_TIDE}}$, Figure 4, right column) are similar to those for SBC speeds (Figure 4, left column). This similarity is consistent with tidal currents providing a significant fraction of SBC energy. However, T_TIDE tidal analysis on one-month data segments may also be influenced by strong inertial currents, as we demonstrate in the following section.

5.3 Harmonic tidal analysis compromised by inertial currents

We demonstrate the potential influence of inertial currents on T_TIDE analyses using time series of simulated wind-driven inertial currents from the damped-slab model described in section 4.3 and including the correction for the presence of sea ice. Time series of inertial currents at the $M1_6$ mooring location (Figure 5, top) were evaluated for SML thicknesses of 10 m and 50 m, roughly representing summer and winter conditions, respectively. For a 10 m SML, simulated inertial currents frequently exceed 20 cm/s in every season, reaching a maximum of 36 cm/s in October 2014. This maximum is similar to maximum measured currents (Figure 2) and SBCs (Figure 4). Modeled values depend on the choice of the damping time scale, which we have taken to be 14 days to maximize the inertial response of the SML; however, sensitivity to the damping scale is weak over a range of several days.

We applied the T_TIDE analysis described in section 4.2 to the slab-model output to produce $|u|_{\mathrm{T\_TIDE}}$, and the associated tidal ellipse parameters. The T_TIDE analysis assigns a substantial portion of the near-inertial energy to S_2* (maximum of 15 cm/s) and M_2 (maximum of 7 cm/s). We attribute the larger amplitude of the S_2* term, relative to M_2, to the proximity of f to the frequency of S_2. The time series of $|u|_{\mathrm{T\_TIDE}}$ has maximum values of about 15 cm/s and is modulated at time scales of roughly two weeks, caused by the superposition of the spurious M_2 and S_2* constituents.

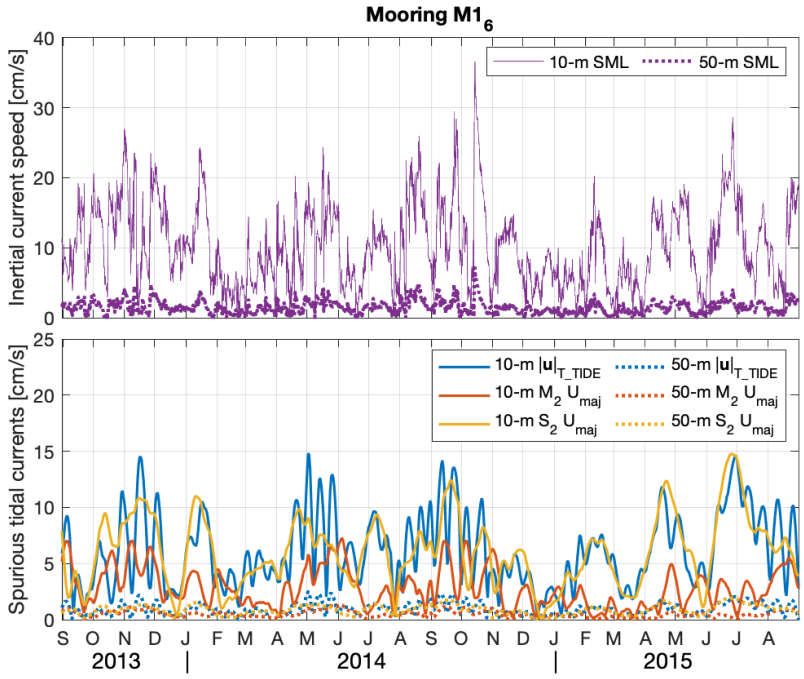

Figure 5. Top: Simulated inertial currents for idealized SML depths of 10 m and 50 m at mooring M1$_6$. Bottom: Output of T_TIDE tidal analysis from the purely inertial time series above.

Simulated inertial currents are much weaker for an idealized 50-m thick SML, seldom exceeding 5 cm/s. Values of $|u|_{\mathrm{T\_TIDE}}$ average 1 cm/s with a maximum of 2.5 cm/s.

We conclude that, for shallow mixed layers during summers, T_TIDE analysis of one-month time intervals of data is substantially affected by wind-forced near-inertial motion, placing strong constraints on our analysis of tidal currents. During winter, however, when the SML is deep and the high-concentration ice cover damps excitation of inertial oscillations, inertial influence on tidal analysis is small and we expect that T_TIDE results represent tides. This is supported by the clear fortnightly oscillations in the SBCs (Figure 4, left), which are expected from spring-neap tidal cycles but inconsistent with the irregular weather-band forcing of inertial waves.

5.4 Tidal properties

With the caveat that strong wind-forced near-inertial oscillations may be misrepresented as tides in T_TIDE analyses on short records, we use time- and depth-dependent

variability of tidal ellipses along the 126°E transect (Figure 6) to identify possible contributions of tides to SBC variability. The ratio of major to minor axis amplitudes ($U_{\mathrm{maj}}/|Umin|$) controls the eccentricity of the tidal ellipses, while the sign of the minor axis amplitude determines the direction of rotation. Note that the sampled depth range varies between moorings.

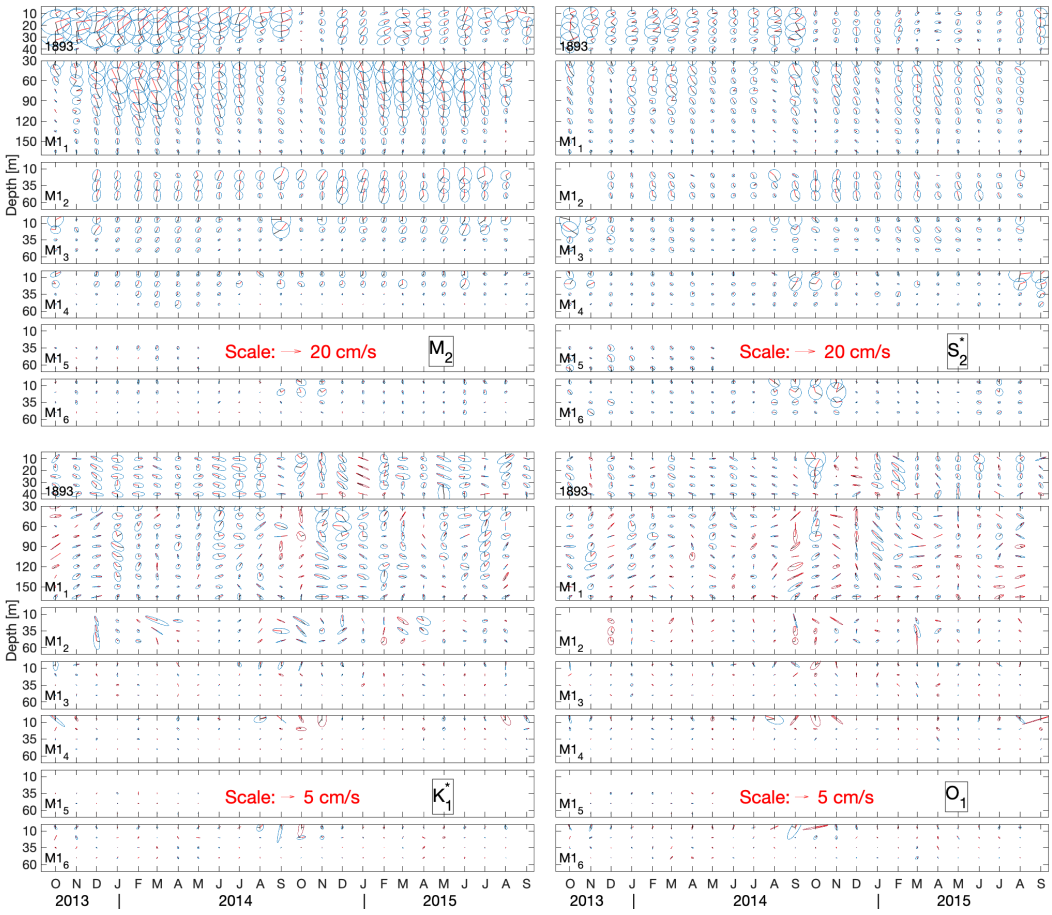

Figure 6. Tidal ellipses from T_TIDE for the leading semidiurnal frequencies (M_2 and S_2*, top) and the diurnal constituents K_1* and O_1 (bottom). Ellipses are interpolated on a monthly grid with 15m vertical resolution. Blue ellipses show clockwise rotation, red ellipses counter-clockwise rotation. Red lines indicate ellipse orientation and black lines indicate Greenwich phase (counter-clockwise from the right). Note the different scales for semidiurnal and diurnal constituents.

For both semidiurnal constituents, ellipses are roughly circular at all moorings, with eccentricities averaging 1.6 and 1.3 for all moorings for M_2 and S_2*, respectively. The ellipses for the diurnal constituents are closer to rectilinear, with eccentricities averag-

ing 3.1 and 3.2 for K_1* and O_1, respectively. However, major axis amplitudes for diurnal constituents are very small ($\leq$1.5 cm/s except for K_1* at 1893), and mostly below the 95% confidence level (see Table 1). Orientations and phases vary widely between the moorings but tend to behave similarly for frequencies that are close together (i.e., for the pairs M_2 and S_2*, and K_1* and O_1). Our T_TIDE analysis of data at mooring $M1_4$ during 2013-2015 (Figure 6) confirms the seasonal variability of M_2 and S_2* reported by Pnyushkov and Polyakov (2012) using older data (2004-2005) obtained at the same location. Throughout the array in 2013-2015, major axis amplitudes of M_2 and S_2* show two patterns of seasonality: wintertime deepening of current maxima (mostly M_2), and summertime surface amplification, especially for S_2* (Figure 7). We reiterate, however, that these results do not necessarily indicate changes in baroclinic tide generation or radiation: strong wind-forced inertial oscillations, especially for shallow SMLs in early summer, likely contaminate T_TIDE estimates of semidiurnal current ellipse properties (Figure 5, and section 5.3).

The pattern of deepening M_2 tidal currents in winter from T_TIDE analysis is most pronounced on the upper slope (mooring $M1_1$) where data are available throughout most of the water column. Deepening started with the freeze-up in late October and reached maximum depth in March for both winters (2013-2014 and 2014-2015), with M_2 major axis amplitudes reaching maxima of about 14 cm/s at around 70 m depth. These values are much greater than the values obtained by T_TIDE analysis of purely wind-forced inertial currents for deep SMLs (Figure 5), indicating that the variability at this mooring is truly tidal. The subsequent shoaling was gradual during spring 2014, interrupted by a temporary additional deepening event in May-June. In spring 2015, the shoaling progressed more quickly and happened almost entirely between mid-June and mid-July. At the peak of the shoaling in summer, the maximum appears to be above the 30 m depth limit of our observations at mooring $M1_1$.

On the shelf, at mooring 1893, a similar seasonality with generally strong tidal currents occurred during the first deployment period (2013-2014). During the second deployment (2014-2015), seasonality was still present, but measured tidal amplitudes were generally much weaker. We are presently unable to explain this abrupt change. At the $M1_2$ mooring 11 km down the slope from $M1_1$, the shape of winter deepening resembles that at mooring $M1_1$, but major axis amplitudes are much lower ($\sim$6 cm/s for the first winter and $\sim$10 cm/s for the second) and the deepening appears to be limited to shal-

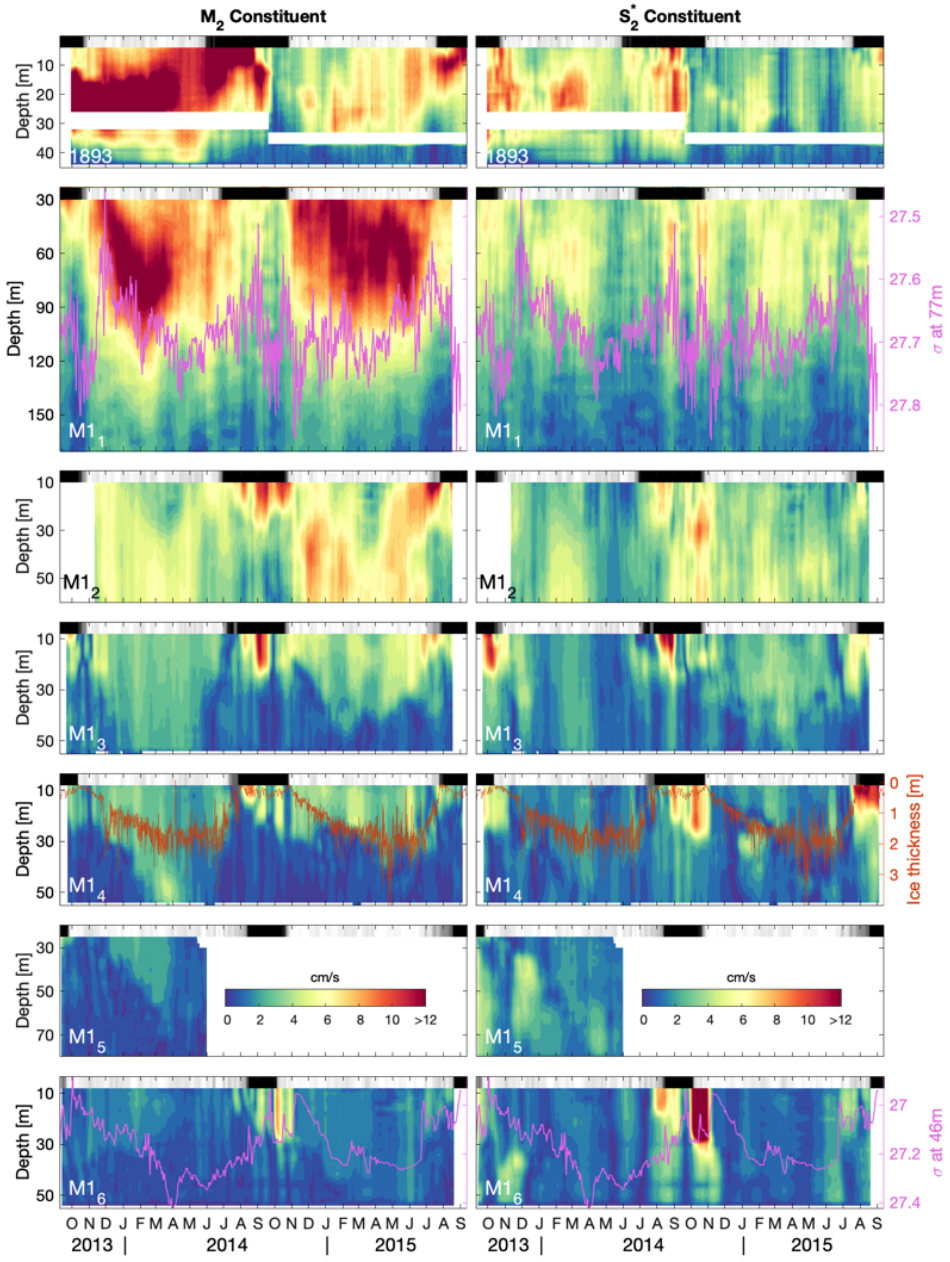

Figure 7. Time-depth plots of major axis amplitudes of the M_2 (left) and S_2* (right) constituents at the moorings across the continental slope. Gray shading at the top of the plots indicates sea-ice concentration (white= 100% , black=0%). Pink lines show detrended potential density (σ) at the shallowest available level (for moorings at which this level is above the deepest ADCP observations) and the red line in the $M1_4$ panel shows sea-ice thickness from upward looking sonar observations (one-day low-pass filtered).

lower depths than at $M1_1$, although below the observational limit of 60 m. Further offshore, the pattern becomes less visible with increased distance from the slope and the depth range of the deepening continues to decrease (reaching only ∼30 m depth during the second winter at mooring $M1_4$).

We propose that this pattern of variability is related to seasonal changes of stratification. At moorings $M1_1$ and $M1_6$, hydrographic records are available within the ADCP depth range, at 77 m for $M1_1$ and 46 m for $M1_6$ (Figure 4). Density time series show a seasonal cycle with increasing density over the course of the winter and decreasing again in spring, which is in phase with the deepening and shoaling of elevated M_2 tidal currents. The limited hydrographic sampling and two-year lengths of the time series restrict our ability to quantitatively determine the relationship between stratification and tidal currents. Nonetheless, the observed seasonal cycle of density qualitatively supports a connection between the tidal amplitudes and stratification as has been shown, for example, by Janout and Lenn (2014) for a site on the Laptev Sea shelf.

Summertime surface amplification is observed at almost all moorings for both constituents (the only exceptions being M_2 at moorings 1893 and $M1_1$) and is most likely dominated by wind-driven inertial currents that are erroneously attributed by the harmonic analysis to tidal constituents. S_2* reaches its greatest major axis amplitude of 18 cm/s at the northernmost $M1_6$ mooring location during October 2014, which is close to the maximum of 15 cm/s that T_TIDE produces from purely inertial input for this mooring (compare Figure 7 and Figure 5).

6 Discussion

6.1 Pronounced seasonality of semidiurnal currents

Our analyses show a clear seasonal cycle of SBCs and $|u|_{\mathrm{T\_TIDE}}$ (Figure 4). We expect that the primary controls on the time and depth distributions of these currents are stratification and sea ice, the latter being a control on the generation of wind-driven inertial oscillations in the SML and the damping of baroclinic tides.

Upper ocean hydrography is directly dependent on the seasonal cycle of sea ice: brine rejection during sea-ice formation leads to an increase of upper ocean density and convection, which causes a deepening of the pycnocline. Conversely, springtime ice melt introduces buoyant freshwater and re-stratifies the upper ocean which is associated with

a shoaling of the pycnocline. The vertical extent of measured SBCs and total tidal currents follow the winter deepening and subsequent springtime shoaling of the pycnocline (Figure 4). We argue that during these times and in these depths, the influence of wind-driven inertial currents is small so that the signals are likely to be of tidal origin. Baroclinic tidal currents are tightly linked to vertical density gradients and thus follows the seasonal evolution of the pycnocline (e.g., Janout & Lenn, 2014).

A baroclinic tidal model (section 4.3) confirms that most near-surface tidal kinetic energy is concentrated on the shelf and at the continental slope (Figure 8). North of the M_2 critical latitude (Figure 1), topographic trapping of the barotropic M_2 tide is expected. This may have important implications for the analysis of baroclinic tidal currents and the calculation of energy fluxes (Musgrave, 2019). Estimates from an idealized 2-D model developed by Hughes and Klymak (2019) suggest that, for the eastern EB continental slope, significant current anomalies associated with trapping are confined to a small area of ∼10 km length at the upper slope close to the sea floor (∼200 m bottom depth, not shown). We thus conclude that for the analysis of widespread (∼550 km cross-slope) upper ocean variability of tidal currents, effects of topographic trapping of the barotropic M_2 tide are small.

The modeled near-surface fields of baroclinic major axis amplitudes (U_{maj}) are spatially patchy, highlighting the dependence of baroclinic tidal currents on topographical features as well as on background stratification. Major upper-ocean tidal hotspots in the region are the shelf areas around 115°E and 140°E, with $U_{maj}(M_2)$ exceeding 15 cm/s for both summer and winter stratification, although they are stronger in summer. Over the slope and deep basin, summer stratification yields slightly higher values of $U_{maj}(M_2)$ compared to winter (Figure 8, top and middle). While most tidal energy is concentrated at the continental slope, the model produces slightly enhanced S_2 tidal currents in the deep basin (as far as mooring $M1_5$) under summertime stratification (Figure 8, top); however, values of $U_{maj}(S_2)$ barely reach 5 cm/s offshore of the slope compared with ∼18 cm/s for our T_TIDE analyses of summer data at the offshore moorings).

Simulated tidal energy fluxes show that the source regions of baroclinic tidal currents are at the steep continental slope (Figure 9). The M_2 internal tide is confined by critical latitude effects and only propagates eastward along the slope, consistent with the findings of Hughes and Klymak (2019) for a subinertial wave. However, the super-inertial

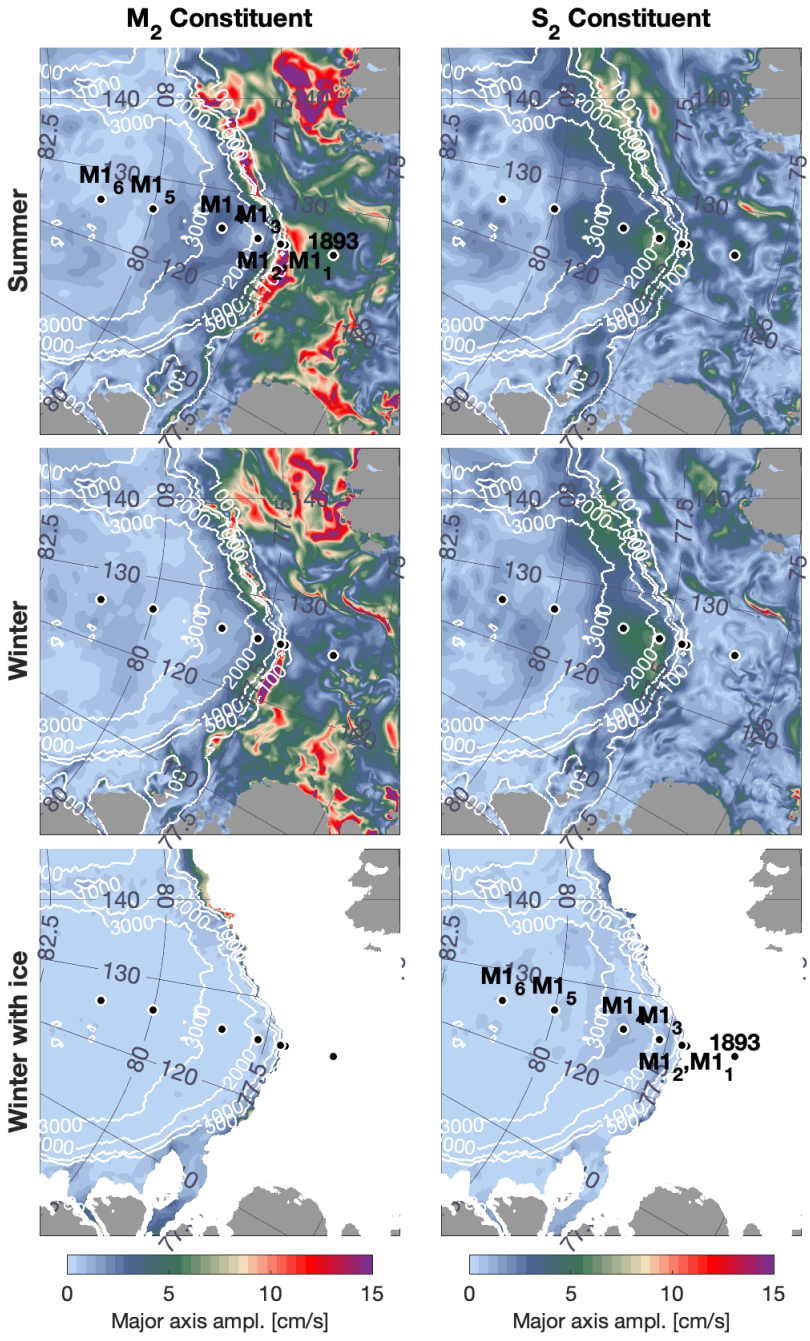

Figure 8. Regional maps of the eastern EB showing simulated surface baroclinic tidal amplitudes of M_2 (left) and S_2 (right) for different realistic background conditions (see section 4.4 for model description): Summer stratification (top), winter stratification without ice (middle) and winter stratification with landfast ice (bottom). For the latter, values for bottom depths shallower than 150 m are omitted because much of the apparent baroclinic signal is associated with the frictional boundary layer under ice in the presence of strong barotropic currents.

498 S_2 internal tidal tide propagates offshore into the deep basin. This demonstrates the pos-
499 sible pathway for enhanced tidal activity into the central basin. However, we reiterate
500 that modeled $U_{maj}(S_2)$ in the upper ocean is much smaller than we obtain from T_TIDE
501 analyses of summer data.

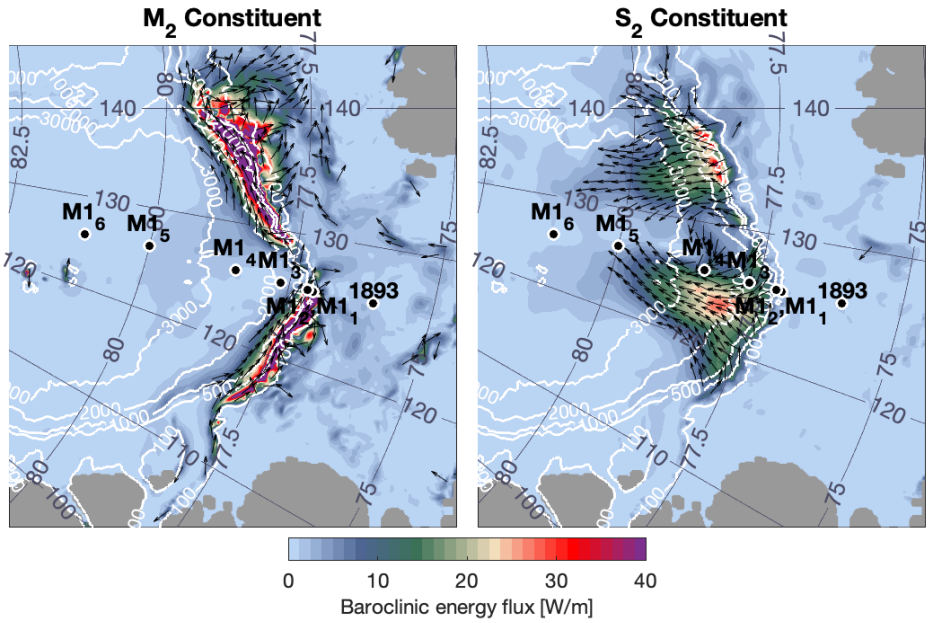

Figure 9. Top: Regional maps of the eastern EB showing vertically integrated horizontal baroclinic energy flux for simulated tidal currents of M_2 (left) and S_2 (right) constituents for summer stratification without sea ice. Colors indicate the amplitude, arrows show the direction of flux higher than 10 W/m. Dots indicate the locations of the moorings across the continental slope.

502 During periods of high ice concentration in winter, SBCs and $|u|_{T\_TIDE}$ often show
503 subsurface maxima, especially on the shelf (mooring 1893) and upper slope (moorings
504 $M1_1$ and $M1_2$, Figure 4). We propose that these patterns are caused by friction at the
505 base of high-concentration ice cover (Morison et al., 1985; D'Asaro & Morison, 1992).
506 In our simulations with winter stratification and a land-fast, thermodynamically passive
507 ice cover providing a frictional surface, near-surface tidal currents are reduced over deep
508 water (Figure 8, bottom), with major axis amplitudes for M_2 being negligible and val-
509 ues for S_2 being less than 2 cm/s. We do not show baroclinic tides for water less than
510 150 m deep for the winter case with ice cover because much of the apparent baroclinic

signal is associated with the frictional boundary layer in the presence of strong barotropic currents.

We conclude that changes in both ocean stratification and ice cover can produce seasonal cycles in baroclinic tides over the deep-water section of our mooring array, but that modeled amplitudes are small compared with measured values. At this time, we do not know if this discrepancy is associated with deficiencies in our tide models or with underestimating the contribution of wind-forced inertial currents to tidal analyses with T_TIDE.

6.2 Limitations of harmonic tidal analysis

As we previously demonstrated (section 5.3, and Figure 5), the proximity of the local inertial frequency to the semidiurnal M_2 and S_2 frequencies prevents a clean analytical separation of the frequencies within a 30-day window. Therefore, we cannot use tidal analysis to unambiguously separate wind-driven inertial variability from time-dependent variability of baroclinic tides.

We conducted further tests in which we applied seasonal tidal analysis with a 90-day window to the simulated inertial time series. This window is sufficiently long to formally separate inertial oscillations from tidal frequencies. Even in this scenario, some inertial energy was erroneously attributed to tidal constituents, arguably due to the broad spread of inertial energy over the semidiurnal band (see spectra in Figure 3).

These tests highlight the limitations of classical harmonic tidal analysis for the study of baroclinic tidal currents within the upper Arctic Ocean, where inertial currents from wind input may be substantial.

7 Summary & Outlook

Analyses of two-year time series of upper-ocean currents from moorings across the continental slope in the eastern Arctic was combined with a slab model of SML near-inertial response to realistic wind stress variability and a three-dimensional baroclinic tide model. The results provide insight into the variability of major sources of upper ocean kinetic energy as sea ice conditions and regional hydrography change through the year. The main findings of this study are as follows:

Table 2. Averages of raw and SBC speed ($|Raw|$ and $|SBC|$, respectively) and their ratio over the whole time and depth domain (same as in Table 1)

All time	$\|Raw\|$ [cm/s]	$\|SBC\|$ [cm/s]	$\|SBC\|/\|Raw\|$ [%]
1893	12.35	8.77	71
$M1_1$	16.14	5.36	33
$M1_2$	12.16	6.23	51
$M1_3$	9.19	4.54	49
$M1_4$	8.41	4.12	49
$M1_5$	4.25	2.71	64
$M1_6$	6.64	3.21	48

- Semidiurnal-band currents (SBCs, 10-14 h period) are a major contributor to kinetic energy in the eastern EB region, with mean SBC speeds being 33-71% of mean total current speeds (Table 2). Tidal currents (dominated by the semidiurnal M_2 and S_2* constituents) are strongest over the upper slope and decrease toward the deep basin.
- During ice-free summer months, SBCs are strongly amplified in the upper ∼30 m, reaching amplitudes in excess of 40 cm/s far offshore in the eastern EB (Figure 4). Between summer periods the depth of strong SBCs varies, following the expected winter deepening and spring shoaling of the pycnocline.
- Models of inertial currents in the SML and baroclinic tide generation and propagation suggest that, while the wintertime SBCs appear to be predominantly of tidal origin, observed large near-surface SBCs in summer in the deep basin are caused primarily by wind forcing of inertial oscillations. However, we predict some contribution from baroclinic tides generated along the upper continental slope (Figs. 8 and 9). Critical latitude effects result in confining the M_2 baroclinic tides to the slope where near-surface currents can be large; however, S_2 tides can radiate northwards into deep water.

- The close proximity of the inertial period to periods of energetic semidiurnal tides and the expected variability of inertial and tidal current phases and amplitudes, precludes the empirical separation of these two signals.

The eastern Arctic Ocean is presently experiencing rapid changes in sea ice and ocean states, including a long-duration summer period free of high-concentration and thick sea ice, and reduced upper-ocean stratification. We speculate that these trends will lead to substantial changes in semidiurnal-band kinetic energy that, in turn, may contribute to the ongoing changes through ocean stress on the sea ice and shear-induced mixing. The long-term changes in SBCs, and the effect on the ocean and sea ice, will depend on the individual and coupled contributions of baroclinic tides and wind-forced inertial oscillations. However, as we have shown, the time-dependence of these signals cannot be separated through purely empirical analysis of mooring data. Instead, we propose that further progress will require dedicated modeling studies that can separate the contributions from both sources of semidiurnal-band currents in a changing Arctic.

Acknowledgments

The mooring data used in this study is available from these references: NABOS currents and hydrography: Polyakov (2016a, 2016b); the German-Russian "Laptev Sea System" mooring 1893: Janout et al. (2019). Atmospheric and sea ice reanalysis data is available from Copernicus Climate Change Service (2017). The ship-based oceanographic observations in the eastern EB and Laptev Sea were conducted under the working frame of the NABOS project with support from NSF (grants AON-1203473 and AON-1338948). Analyses presented in this paper are supported by NSF grants 1249133 and 1249182. TMB was supported in part by a UAF Global Change Student Research Grant award with funds from the Cooperative Institute for Alaska Research. This work used the Extreme Science and Engineering Discovery Environment (XSEDE, Towns et al. (2014)), which is supported by National Science Foundation grant ACI-1548562. In particular, it used the Comet system at the San Diego Supercomputing Center (SDSC) through allocation TG-DPP180004.

References

Aagaard, K. (1989). A synthesis of the Arctic Ocean circulation. *Rapp. P.-v. Rcun. Cons. int. Explor. Mer*, *188*(1), 11–22.

Alford, M. H. (2001). Internal swell generation: The spatial distribution of energy flux from the wind to mixed layer near-inertial motions. *Journal of Physical Oceanography*, *31*(8), 2359-2368. Retrieved from `https://doi.org/10.1175/1520-0485(2001)031<2359:ISGTSD>2.0.CO;2` doi: 10.1175/1520-0485(2001)031⟨2359:ISGTSD⟩2.0.CO;2

Andreas, E. L., Horst, T. W., Grachev, A. A., Persson, P. O. G., Fairall, C. W., Guest, P. S., & Jordan, R. E. (2010, April). Parametrizing turbulent exchange over summer sea ice and the marginal ice zone. *Quarterly Journal of the Royal Meteorological Society*, *136*(649), 927–943.

Beckmann, A., & Haidvogel, D. B. (1993). Numerical simulation of flow around a tall isolated seamount. part i: Problem formulation and model accuracy. *Journal of Physical Oceanography*, *23*(8), 1736-1753. Retrieved from `https://doi.org/10.1175/1520-0485(1993)023<1736:NSOFAA>2.0.CO;2` doi: 10.1175/1520-0485(1993)023⟨1736:NSOFAA⟩2.0.CO;2

Carmack, E., Polyakov, I., Padman, L., Fer, I., Hunke, E., Hutchings, J., ... Winsor, P. (2015, December). Toward Quantifying the Increasing Role of Oceanic Heat in Sea Ice Loss in the New Arctic. *Bulletin of the American Meteorological Society*, *96*(12), 2079–2105.

Coachman, L. K., & Barnes, C. A. (1963, January). The Movement of Atlantic Water in the Arctic Ocean. *Arctic*, *16*(1), 8–16.

Cole, S. T., Toole, J. M., Rainville, L., & Lee, C. M. (2018, August). Internal Waves in the Arctic: Influence of Ice Concentration, Ice Roughness, and Surface Layer Stratification. *Journal of Geophysical Research: Oceans*, *123*(8), 5571–5586.

Copernicus Climate Change Service, C. (2017). *ERA5: Fifth generation of ECMWF atmospheric reanalyses of the global climate* [Data set]. Copernicus Climate Change Service Climate Data Store (CDS). Retrieved from `https://cds.climate.copernicus.eu/cdsapp#!/home`

Danielson, S., & Kowalik, Z. (2005, October). Tidal currents in the St. Lawrence Island region. *Journal of Geophysical Research: Oceans*, *110*(C10), 153.

D'Asaro, E. A. (1985, August). The Energy Flux from the Wind to Near-Inertial Motions in the Surface Mixed Layer. *Journal of Physical Oceanography*, *15*(8), 1043–1059.

D'Asaro, E. A., & Morison, J. H. (1992, September). Internal waves and mixing in

the Arctic Ocean. *Deep Sea Research Part A. Oceanographic Research Papers*, *39*(2), S459–S484.

Dosser, H. V., & Rainville, L. (2016). Dynamics of the changing near-inertial internal wave field in the arctic ocean. *Journal of Physical Oceanography*, *46*(2), 395-415. Retrieved from `https://doi.org/10.1175/JPO-D-15-0056.1` doi: 10.1175/JPO-D-15-0056.1

Falahat, S., & Nycander, J. (2015). On the generation of bottom-trapped internal tides. *Journal of Physical Oceanography*, *45*(2), 526-545. Retrieved from `https://doi.org/10.1175/JPO-D-14-0081.1` doi: 10.1175/JPO-D-14-0081.1

Fer, I. (2014, August). Near-Inertial Mixing in the Central Arctic Ocean. *Journal of Physical Oceanography*, *44*(8), 2031–2049.

Fer, I., Müller, M., & Peterson, A. K. (2015). Tidal forcing, energetics, and mixing near the Yermak Plateau. *Ocean Science*, *11*(2), 287–304.

Fer, I., Skogseth, R., & Geyer, F. (2010, July). Internal Waves and Mixing in the Marginal Ice Zone near the Yermak Plateau. *Journal of Physical Oceanography*, *40*(7), 1613–1630.

Foreman, M. (1978). *Manual for tidal currents analysis and prediction* (Tech. Rep.). Institute of Ocean Sciences, Patricia Bay, Sidney, BC.

Gimbert, F., Marsan, D., Weiss, J., Jourdain, N. C., & Barnier, B. (2012, October). Sea ice inertial oscillations in the Arctic Basin. *The Cryosphere*, *6*(5), 1187–1201.

Gonella, J. (1972, December). A rotary-component method for analysing meteorological and oceanographic vector time series. *Deep Sea Research and Oceanographic Abstracts*, *19*(12), 833–846.

Haidvogel, D. B., Arango, H. G., Hedstrom, K., Beckmann, A., Malanotte-Rizzoli, P., & Shchepetkin, A. F. (2000, August). Model evaluation experiments in the North Atlantic Basin: simulations in nonlinear terrain-following coordinates. *Dynamics of Atmospheres and Oceans*, *32*(3-4), 239–281.

Holloway, G., & Proshutinsky, A. (2007, March). Role of tides in Arctic ocean/ice climate. *Journal of Geophysical Research*, *112*(C4), 3069–3010.

Hughes, K. G., & Klymak, J. M. (2019, May). Tidal Conversion and Dissipation at Steep Topography in a Channel Poleward of the Critical Latitude. *Journal of*

Physical Oceanography, *49*(5), 1269–1291.

Jakobsson, M., Mayer, L., Coakley, B., Dowdeswell, J. A., Forbes, S., Fridman, B., ... Weatherall, P. (2012, June). The International Bathymetric Chart of the Arctic Ocean (IBCAO) Version 3.0. *Geophysical Research Letters*, *39*(12).

Janout, M., Hölemann, J. A., Timokhov, L., & Kassens, H. (2019). *Moored measurements of current, temperature and salinity on the Laptev Sea shelf in 2013-2014* [data set]. PANGAEA. Retrieved from `https://doi.org/10.1594/PANGAEA.908837` doi: 10.1594/PANGAEA.908837

Janout, M. A., & Lenn, Y.-D. (2014, January). Semidiurnal Tides on the Laptev Sea Shelf with Implications for Shear and Vertical Mixing. *Journal of Physical Oceanography*, *44*(1), 202–219.

Kozlov, I., Kudryavtsev, V., Zubkova, E., Atadzhanova, O., Zimin, A., Romanenkov, D., ... Chapron, B. (2017). SAR observations of internal waves in the Russian Arctic seas. In *Igarss 2015 - 2015 ieee international geoscience and remote sensing symposium* (pp. 947–949). IEEE.

Kulikov, E. A. (2004). Barotropic and baroclinic tidal currents on the Mackenzie shelf break in the southeastern Beaufort Sea. *Journal of Geophysical Research*, *109*(C5), 307.

Lenn, Y.-D., Rippeth, T. P., Old, C. P., Bacon, S., Polyakov, I., Ivanov, V., & Hölemann, J. (2011, March). Intermittent Intense Turbulent Mixing under Ice in the Laptev Sea Continental Shelf. *Journal of Physical Oceanography*, *41*(3), 531–547.

Levine, M. D., Paulson, C. A., & Morison, J. H. (1985). Internal waves in the arctic ocean: Comparison with lower-latitude observations. *Journal of Physical Oceanography*, *15*(6), 800-809. Retrieved from `https://doi.org/10.1175/1520-0485(1985)015<0800:IWITAO>2.0.CO;2` doi: 10.1175/1520-0485(1985)015⟨0800:IWITAO⟩2.0.CO;2

Losch, M., Menemenlis, D., Campin, J.-M., Heimbach, P., & Hill, C. (2010, January). On the formulation of sea-ice models. Part 1: Effects of different solver implementations and parameterizations. *Ocean Modelling*, *33*(1-2), 129–144.

Marshall, J., Adcroft, A., Hill, C., Perelman, L., & Heisey, C. (1997, March). A finite-volume, incompressible Navier Stokes model for studies of the ocean on parallel computers. *Journal of Geophysical Research: Oceans*, *102*(C3),

687 5753–5766.

688 Martini, K. I., Simmons, H. L., Stoudt, C. A., & Hutchings, J. K. (2014). Near-
689 inertial internal waves and sea ice in the beaufort sea. *Journal of Physical*
690 *Oceanography*, *44*(8), 2212-2234. Retrieved from `https://doi.org/10.1175/`
691 `JPO-D-13-0160.1` doi: 10.1175/JPO-D-13-0160.1

692 Morison, J. H., Long, C. E., & Levine, M. D. (1985, November). Internal wave dissi-
693 pation under sea ice. *Journal of Geophysical Research: Oceans*, *90*(C6), 11959–
694 11966.

695 Munk, W. (1997, January). Once again: once again—tidal friction. *Progress in*
696 *Oceanography*, *40*(1-4), 7–35.

697 Munk, W., & Wunsch, C. (1998, December). Abyssal recipes II: energetics of tidal
698 and wind mixing. *Deep-Sea Research Part I*, *45*(12), 1977–2010.

699 Musgrave, R. C. (2019, December). Energy Fluxes in Coastal Trapped Waves. *Jour-*
700 *nal of Physical Oceanography*, *49*(12), 3061–3068.

701 Nguyen, A. T., Ocaña, V., Garg, V., Heimbach, P., & Toole, J. M. (2017). On
702 the benefit of current and future ALPS data for improving Arctic coupled
703 ocean-sea ice state estimation. *Oceanography*, *30*(2).

704 Padman, L., & Erofeeva, S. (2004, January). A barotropic inverse tidal model for
705 the Arctic Ocean. *Geophysical Research Letters*, *31*(2), 53–4.

706 Padman, L., Plueddemann, A. J., Muench, R. D., & Pinkel, R. (1992, August).
707 Diurnal tides near the Yermak Plateau. *Journal of Geophysical Research:*
708 *Oceans*, *97*(C8), 12639–12652.

709 Padman, L., Siegfried, M. R., & Fricker, H. A. (2018, March). Ocean Tide Influences
710 on the Antarctic and Greenland Ice Sheets. *Reviews of Geophysics*, *56*(1),
711 142–184.

Pawlowicz, R., Beardsley, B., & Lentz, S. (2002, October). Classical tidal harmonic analysis including error estimates in MATLAB using T_TIDE. *Computers & Geosciences*, *28*(8), 929 – –937.

712 Pnyushkov, A. V., & Polyakov, I. V. (2012, January). Observations of Tidally In-
713 duced Currents over the Continental Slope of the Laptev Sea, Arctic Ocean.
714 *Journal of Physical Oceanography*, *42*(1), 78–94.

715 Pnyushkov, A. V., Polyakov, I. V., Ivanov, V. V., Aksenov, Y., Coward, A. C.,
716 Janout, M., & Rabe, B. (2015, July). Structure and variability of the bound-

ary current in the Eurasian Basin of the Arctic Ocean. *Deep Sea Research Part I: Oceanographic Research Papers*, *101*, 80–97.

Pnyushkov, A. V., Polyakov, I. V., Ocean, R. R., Ivanov, V. V., Alkire, M. B., Ashik, I. M., ... Sundfjord, A. (2018). Heat, salt, and volume transports in the eastern Eurasian Basin of the Arctic Ocean from 2 years of mooring observations. *Ocean Science*, *14*, 1349–1371.

Pollard, R. T., & Millard Jr, R. C. (1970, August). Comparison between observed and simulated wind-generated inertial oscillations. *Deep Sea Research and Oceanographic Abstracts*, *17*(4), 813–821.

Polyakov, I. V. (2016a). *Nabos ii - adcp water current data 2013 - 2015* [data set]. Arctic Data Center. Retrieved from `https://arcticdata.io/catalog/view/doi:10.18739/A2RS9B` doi: doi:10.18739/A2RS9B

Polyakov, I. V. (2016b). *Nabos ii - mooring data 2013 - 2015* [data set]. Arctic Data Center. Retrieved from `https://arcticdata.io/catalog/view/doi:10.18739/A2N37R` doi: doi:10.18739/A2N37R

Polyakov, I. V., Pnyushkov, A. V., Alkire, M. B., Ashik, I. M., Baumann, T. M., Carmack, E. C., ... Yulin, A. (2017, April). Greater role for Atlantic inflows on sea-ice loss in the Eurasian Basin of the Arctic Ocean. *Science*.

Polyakov, I. V., Rippeth, T., Fer, I., Baumann, T., Carmack, E., Ivanov, V., ... Rember, R. (submitted). Transition to a New Ocean Dynamic Regime in the Eastern Arctic Ocean. *Geophysical Research Letters*.

Prinsenberg, S. J., & Bennett, E. B. (1989). Vertical variations of tidal currents in shallow land fast ice-covered regions. *Journal of Physical Oceanography*, *19*(9), 1268-1278. Retrieved from `https://doi.org/10.1175/1520-0485(1989)019<1268:VVOTCI>2.0.CO;2` doi: 10.1175/1520-0485(1989)019⟨1268:VVOTCI⟩2.0.CO;2

Rainville, L., & Woodgate, R. A. (2009, December). Observations of internal wave generation in the seasonally ice-free Arctic. *Geophysical Research Letters*, *36*(23), 1487–5.

Rippeth, T. P., Lincoln, B. J., Lenn, Y.-D., Green, J. A. M., Sundfjord, A., & Bacon, S. (2015, March). Tide-mediated warming of Arctic halocline by Atlantic heat fluxes over rough topography. *Nature Geoscience*, *8*(3), 191.

Rippeth, T. P., Vlasenko, V., Stashchuk, N., Scannell, B. D., Green, J. A. M., Lin-

coln, B. J., & Sheldon Bacon. (2017). Tidal conversion and mixing poleward of the critical latitude (an Arctic case study). *Journal of Geophysical Research*.

Rudels, B., Jones, E. P., Anderson, L. G., & Kattner, G. (1994). On the Intermediate Depth Waters of the Arctic Ocean. In *The polar oceans and their role in shaping the global environment* (pp. 33–46). Washington, D. C.: American Geophysical Union.

Shchepetkin, A. F., & McWilliams, J. C. (2005, January). The regional oceanic modeling system (ROMS): a split-explicit, free-surface, topography-following-coordinate oceanic model. *Ocean Modelling*, *9*(4), 347–404.

Simmons, H. L., Hallberg, R. W., & Arbic, B. K. (2004, December). Internal wave generation in a global baroclinic tide model. *Deep Sea Research Part II: Topical Studies in Oceanography*, *51*(25-26), 3043–3068.

Timofeev, V. T. (1960). Water Masses of the Arctic Basin. *Gidrometeoizdat*, p. 190.

Towns, J., Cockerill, T., Dahan, M., Foster, I., Gaither, K., Grimshaw, A., ... Wilkins-Diehr, N. (2014, Sep.). Xsede: Accelerating scientific discovery. *Computing in Science Engineering*, *16*(5), 62-74. doi: 10.1109/MCSE.2014.80

Wunsch, C. (1975, February). Internal tides in the ocean. *Reviews of Geophysics*, *13*(1), 167–182.